Supporting Information

Kinetics and Dynamics of Atomic-Layer Dissolution on Low-Defect Ag

Yufei Wang,[1] Roberto Garcia-Carrillo,[1] Hang Ren [1,2,3,*]

1. Department of Chemistry, 2. Center for Electrochemistry, 3. Texas Materials Institute, The University of Texas at Austin, Austin, TX 78712, USA

* Corresponding author: hren@utexas.edu

Table of Contents

1. Microparticle deposition

Silver microparticles were deposed using a potentiostat (650C, CH Instruments). A capillary (I.D. 0.08″, O.D. 0.12″) containing an electrolyte solution of 6 M $AgNO_3$ and 100 mM HNO_3 was positioned above a glassy carbon plate electrode. A silver wire, serving as the combined reference and counter electrode, was immersed in the electrolyte solution. An applied potential of -20 mV vs Ag/Ag^+ was maintained for 100 seconds during the electrodeposition process, resulting in the nucleation and growth of numerous silver particles on the substrate. The deposited Ag microparticles were examined using both optical and electron microscopy. Among these, particles exhibiting single crystal facets were selected for further SECCM dissolution experiments.

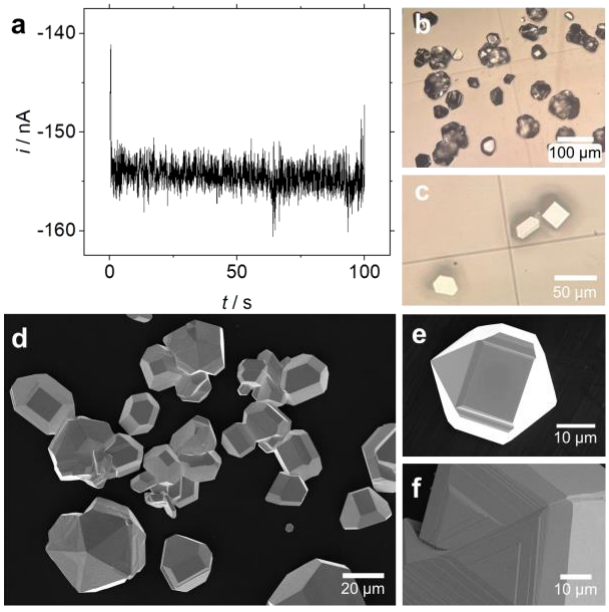

Figure S1. (a) Example *i*-t curve for constant potential deposition of microparticles. (b) Optical image of deposited microparticles on glassy carbon. (c) Zoomed-in optical image of the microparticle shape, which suggests different surface facets. (d) SEM of deposited microparticles on glassy carbon. (e-f) Zoomed in SEM of the microparticles.

2. Extended experimental section

Pipette preparation and characterization

Nanopipettes were fabricated from quartz capillary (1.0 mm o.d., 0.7 mm i.d., Sutter) using a laser-heated capillary puller (Sutter, P-2000). The program used was HEAT=500, FIL=1, VEL=30, DEL=145, PUL=175. The opening size of the pipette was measured by scanning electron microscopy (Quanta 650). The image was taken under 10 keV accelerated voltage and 10 mm working distance.

Scanning electrochemical cell microscopy (SECCM)

The SECCM experiment was performed on a custom-built scanning electrochemical probe system. All experiments were conducted in a solution containing 1 mM $AgClO_4$ and 10 mM $HClO_4$. The presence of Ag+ in the solution helps establish a well-defined equilibrium potential.

The x-y direction movement of the pipette was controlled by a two-axis piezo (P-621-2CD, PI). The vertical movement of the pipette was controlled by a three-axis piezo (P-753 3CD, PI). The piezo system was set up on a Minus K vibration isolation table and enclosed in a Faraday cage with acoustic isolation. Constant current was applied using a patch-clamp amplifier (EPC 10 USB, HEKA). Instrument control and data acquisition were interfaced by the WEC-SPM software developed by the Unwin group.[1] The potential signal was filtered using a 2-pole 3.8 kHz Bessel filter. It was sampled every 4 µs and averaged every 129 data points, giving an effective sampling frequency of 1.97 kHz.

Hopping mode was employed in the scan, and potential was used as the feedback. The same applied current was repeated on a row, and the current was varied between the rows. Within each row, the stepping distance was chosen to avoid overlap between the measurement, ensuring the dissolution occurs on a local area on the Ag microparticle where electrodissoluton has not occurred.

3. Microparticle quality characterization

The quality of the silver microparticle surfaces was assessed by AFM scanning of the basal plane. The RMS roughness of 977 pm is obtained, indicating a low surface roughness on the exposed facet. This level of roughness suggests a low density of microstructural irregularities.

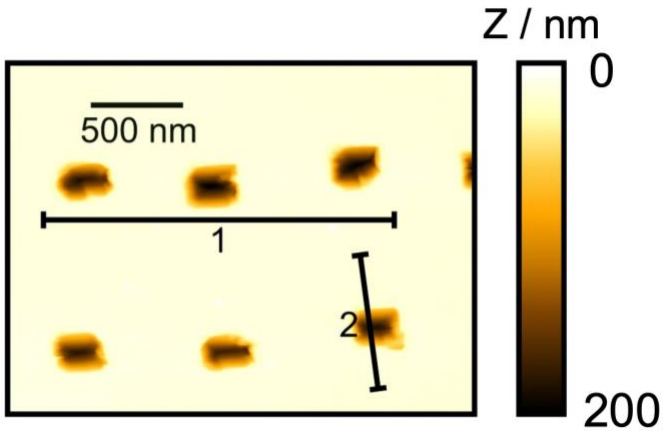

Figure S2. Contact AFM measurements of the basal plane and dissolution area in a (100) surface.

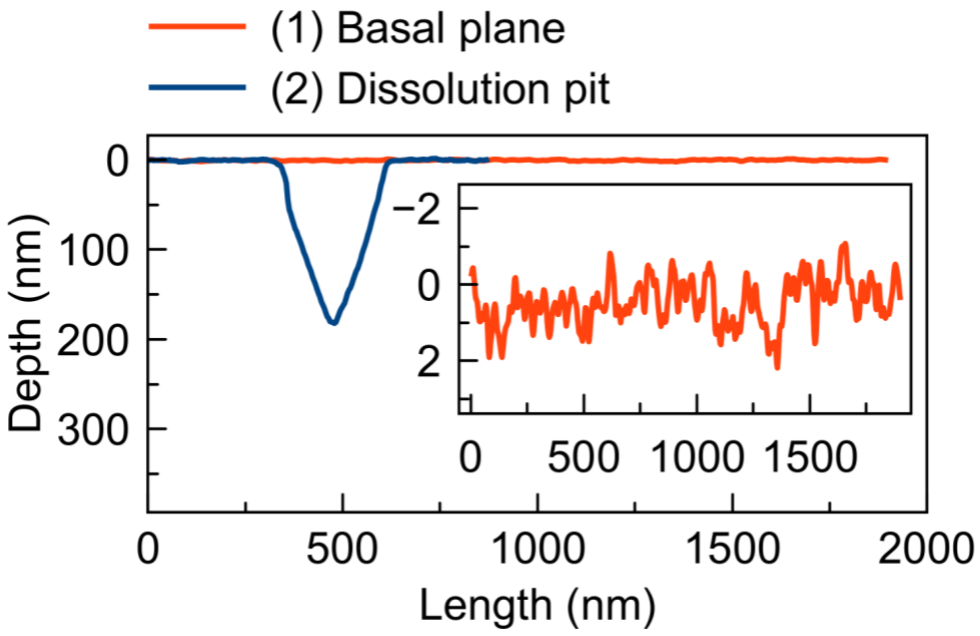

Figure S3.Contact AFM profile of basal plane vs dissolution area in a (100) surface.

4. Examples of *E-t* curves on Ag (111) and (100) surfaces

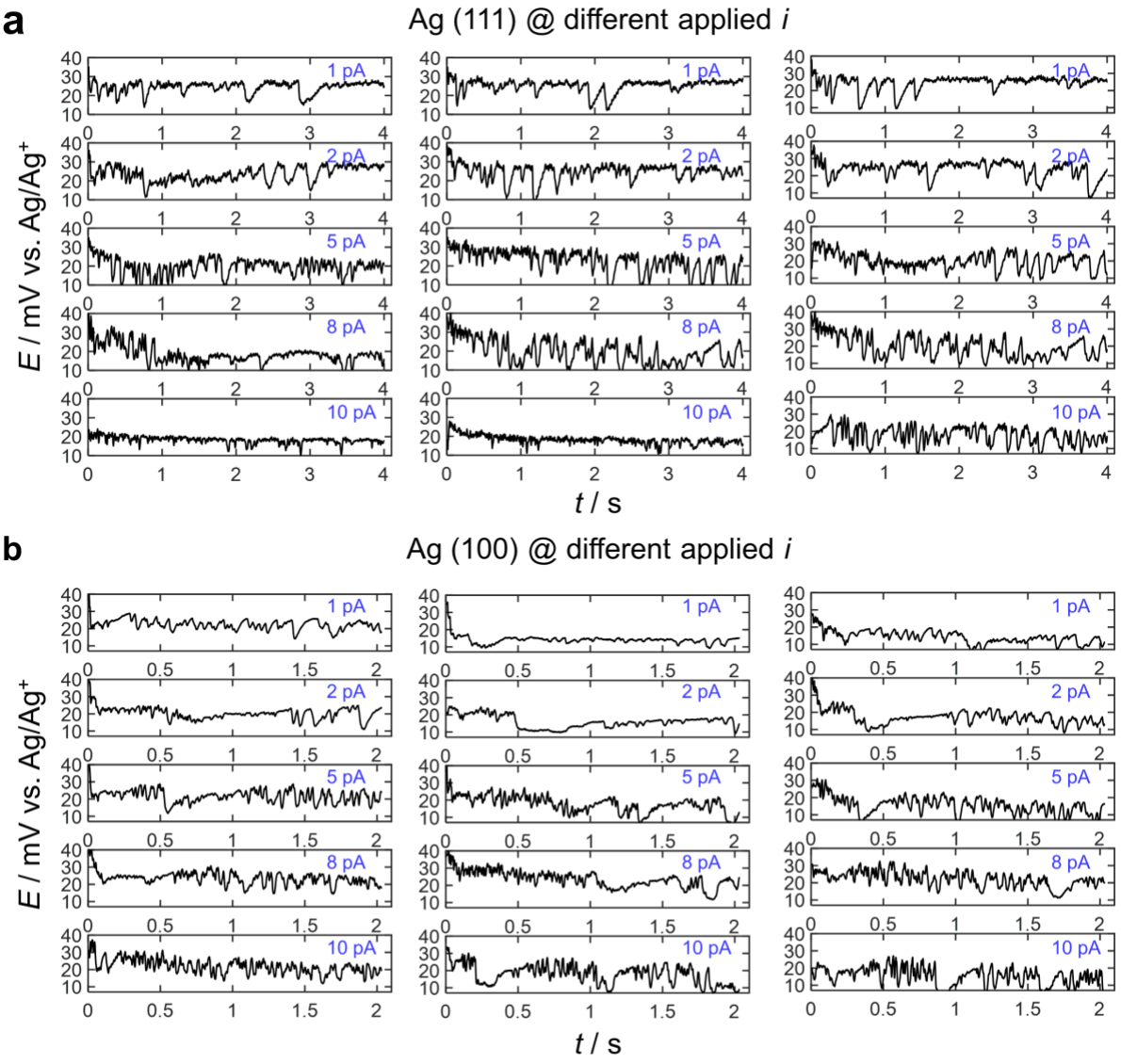

Figure S4. (a) Examples *of E-t* curves on Ag (111) at different applied currents. (b) Examples of *E-t* curves on Ag (100) at different applied currents. Three *E-t* curves were shown under each condition.

5. Ag dissolution with different durations

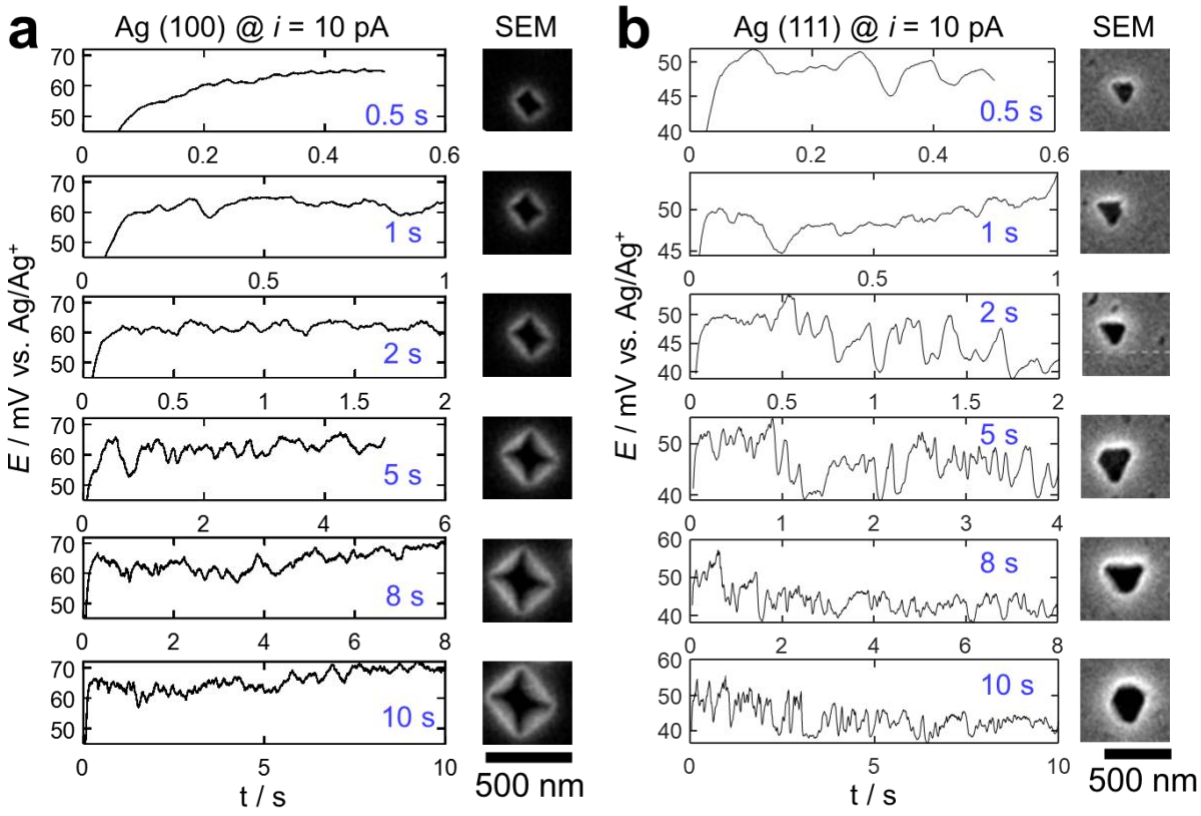

Figure S5: Representative *E-t* curve illustrating the dissolution at 10 pA for different durations on (a) Ag (100) and (b) Ag (111). Corresponding SEM images on the right show the resulting dissolution pits.

6. Charge and shape of dissolution pits

AFM was applied to measure the topography of the dissolution pits in Figures 2b and 2e in the main text. The charge from the constant current experiment is calculated via:

$$Q = i_{\mathrm{app}} t \qquad \text{S-1}$$

Where Q is the charge from the constant current experiment at an applied current of i_{app}. The dissolution charge based on the geometry measured from AFM is calculated following Faraday's law of electrolysis:

$$Q_{\mathrm{diss}} = 4zFV/V_{\mathrm{m}} \qquad \text{S-2}$$

Where the V is the volume of the dissolution pit, $z = 1$ is electron transfer for Ag^0 to Ag^+, F is Faraday's constant, V_{m} = 10.1 cm^3 / mol is the molar volume Ag, which is calculated using the FCC unit cell of Ag.

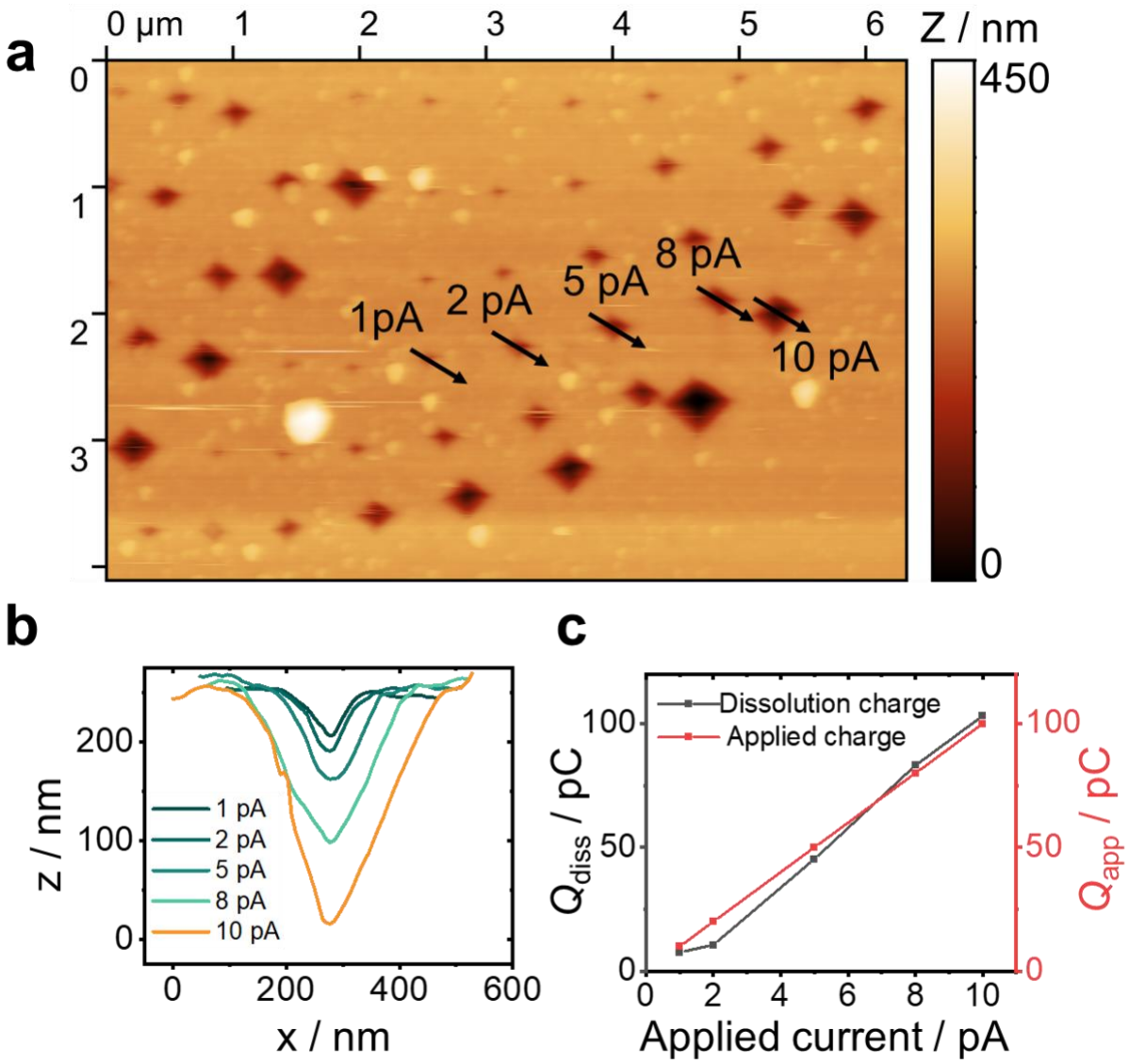

Figure S6: (a) AFM topography map of the dissolution pits in Figure 2a in the main text. (b) The line-scan profiles of the Ag dissolution pit after dissolution formed at various applied currents for 10 s as indicated by the black arrows in (a). (c) Applied charge (Q_{app}) vs the charge derived from the volume of the dissolution pit (Q_{diss}).

7. Theoretical charge of a monolayer

When the surface crystallographic orientation of the silver crystal is (100), the dissolution proceeds as a growing pit with inverted square pyramidal morphology, exposing (111) facets as shown in Figure S7a. As shown in Figure S7b, the number of exposed atoms within the (111) planes is 13 after the initial dissolution step. The dissolution continuing into the subsequent layers results in 41 surface atoms (Figure S7c), and 65 surface atoms (Figure S7d). Following this trend, the number of exposed atoms per layer of dissolution is described by:

$$N_n = N_{n-1} + 8(n+1) \quad \text{S-3}$$

Where N_n is the number of silver atoms at the surface of the exposed (111) planes at the nth layer of dissolution.

By relating N_n, the surface area of the dissolution pit obtained by AFM, S_{AFM}, (Figure S6b) and the planar density of Ag along (111) plane, ρ_{111}, the theoretical charge per monolayer, Q_n, can be obtained using the following equations:

$$N_n = \rho_{111} S_{AFM} \quad \text{S-4}$$

$$Q_n = N_n e \quad \text{S-5}$$

In eq 5, e is the elemental charge. The resulting values for different applied currents are shown in Figure S8 (blue). The average charge per monolayer can also be calculated from the constant current experiment via equation S-1, multiplying the average period between oscillation potential, Δt (Figure 4c), and the applied current, shown in Figure S8 (red).

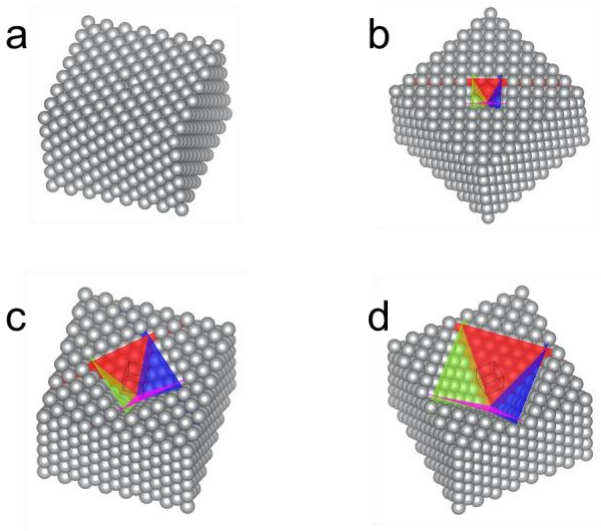

Figure S7. The pyramid dissolution pits on Ag (100) after dissolving (a) 0 (b) 1 (c) 2, and (d) 3 layers.

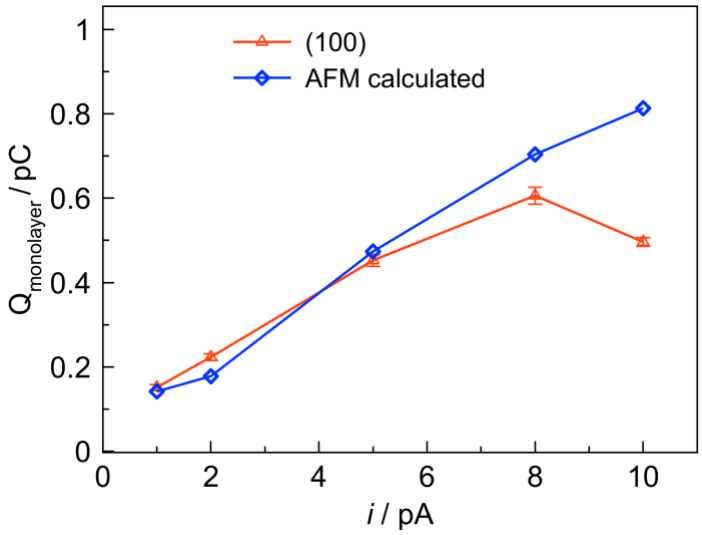

Figure S8. Average charge calculated for a single potential oscillation during the dissolution on Ag (100) (red) vs. calculated expected charge of the last monolayer (blue) from AFM measurements at various applied currents.

8. Peak analysis for *E-t* curve

To analyze the oscillation period in the potential transient, the 60 Hz noise in the raw data was first digitally filtered using a notch filter (59-61 Hz) in MATLAB. The *E-t* curve and the frequency spectrum after fast Fourier transform (FFT) with and without filtering are shown in Figure S9a-b. Peak finding was performed using the "findpeaks" function in MATLAB. The peak widths are measured from the peak finding as shown in Figure S9c.

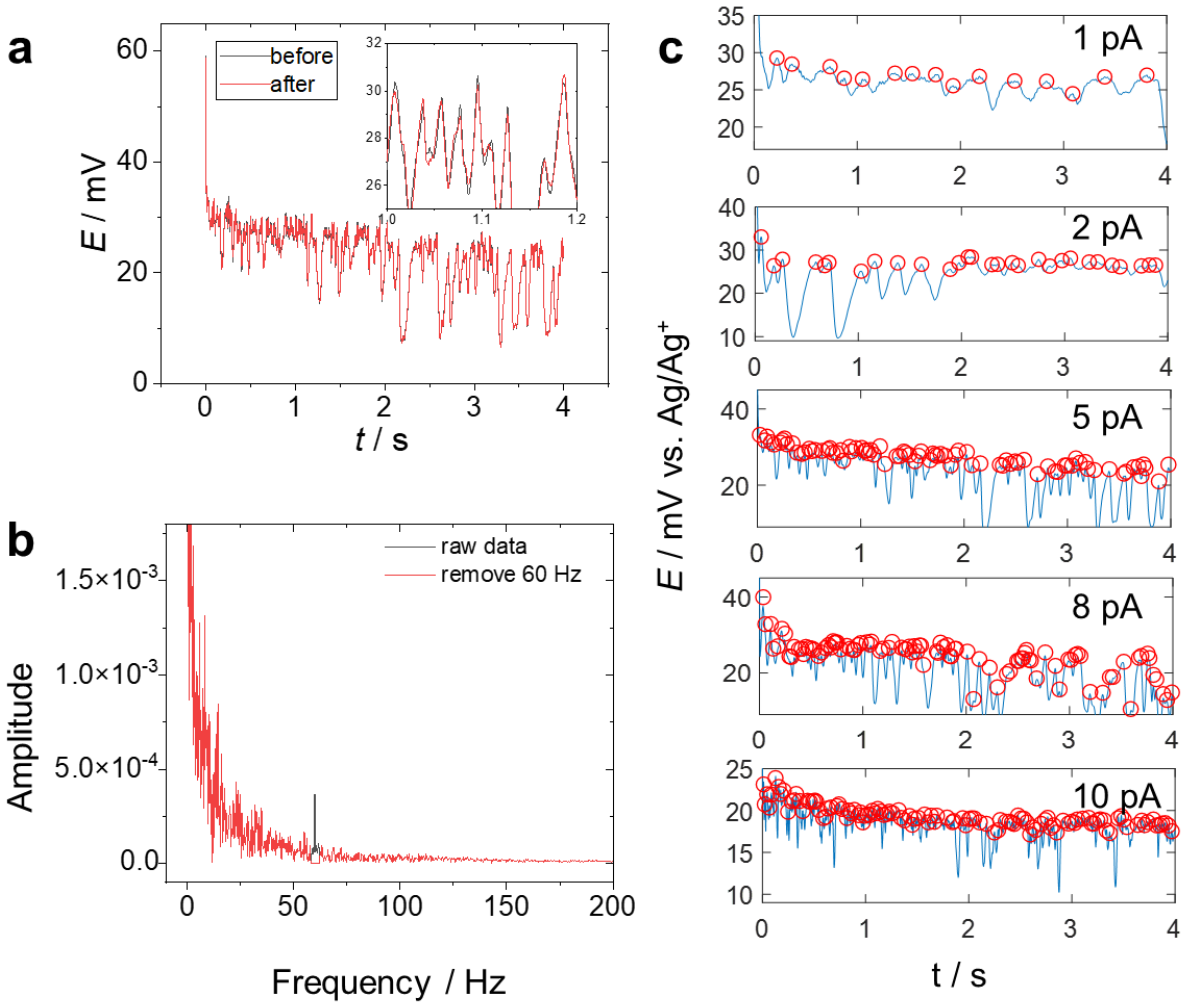

Figure S9. (a) *E-t* curve and (b) the corresponding frequency spectrum before (blue) and after (red) applying the 60-Hz notch filter. (c) Example of peak finding in *E-t* curves. The peak positions are labeled with red circles.

9. Experiments under N_2 and O_2 atmospheres.

To rule out alternative dissolution dynamics, particularly those involving oxide formation, which can lead to active dissolution and passivation, we conducted constant current experiments under controlled N_2 and O_2 atmospheres. As shown in Figure S10, the potential oscillation behavior remains consistent under both N_2 and O_2 atmospheres, confirming that oxygen does not influence the dissolution dynamics.

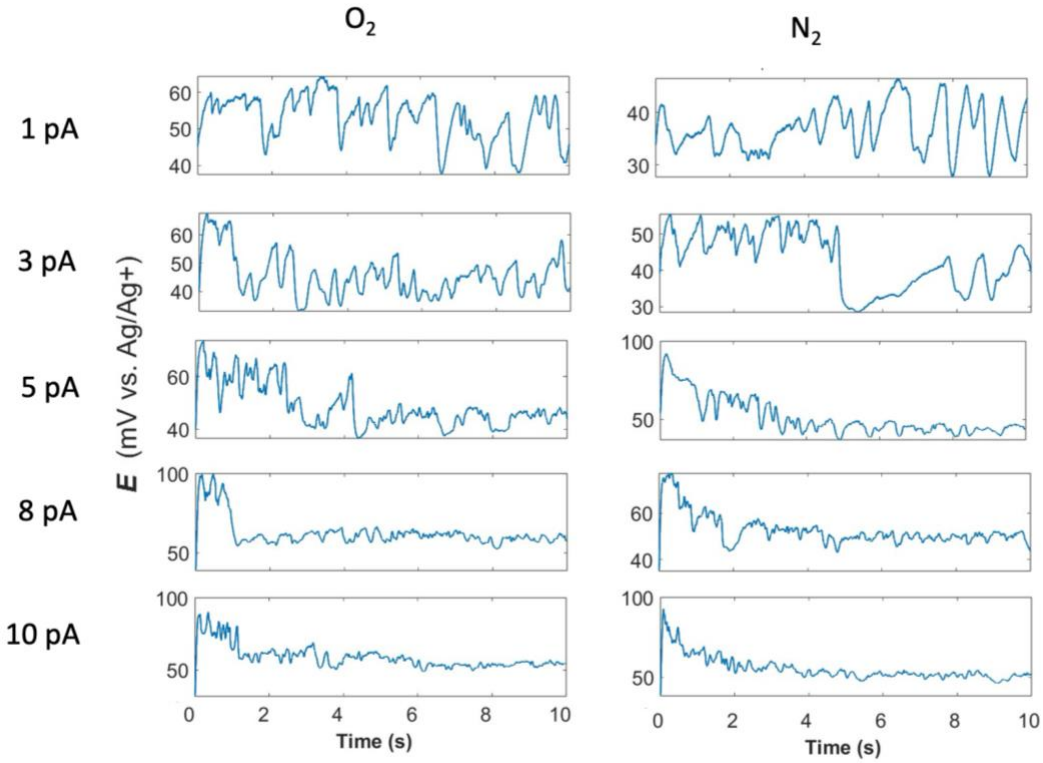

Figure S10. Galvanostatic dissolution experiment on a (100) surface under saturated O_2 (right) and N_2 (left) atmospheres at different applied currents.

10. EIS measurements

Electrochemical Impedance Spectroscopy (EIS) was first performed on a model circuit (EPC 10, HEKA, circuit model shown in Figure S11a) to validate the performance of the patch clamp amplifier. A sinusoidal potential stimulus with a frequency range of 10 Hz to 3.5 kHz and an amplitude of 10 mV was applied to the model circuit. The impedance result for the model circuit is shown in Figure S11b, which agrees very well with the expected response based on simulation using the circuit model.

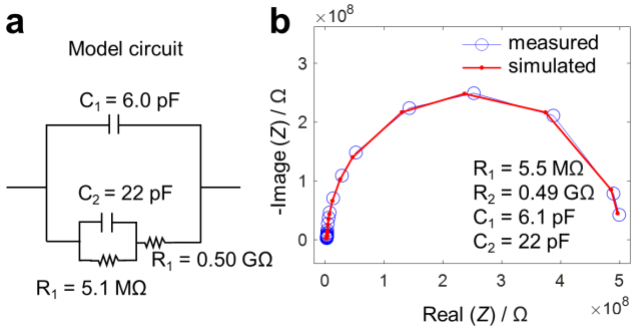

Figure S11. (a) Model circuit diagram (MC 10, HEKA). (b) Nyquist plot of the measured impedance from the model circuit. Blue circle: experimental data. Red line: fitting. The fitted parameters are labeled in the inset.

We also further validated the amplifier's response by a current step experiment using the model circuit, as shown in Figure S12. The response in Figure S12b shows that the amplifier's response time in the galvanostatic mode is less than 1 ms.

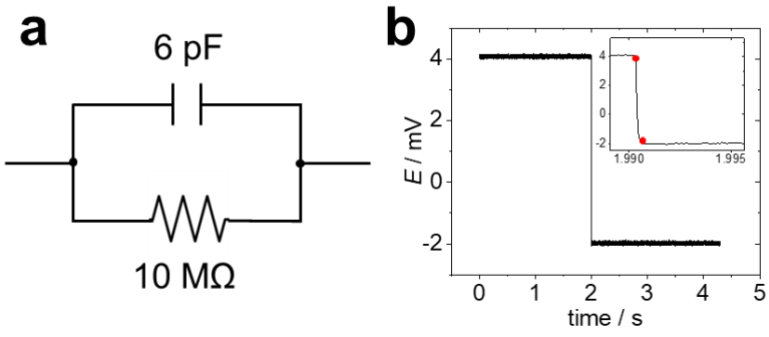

Figure S12. (a) Model circuit diagram. (b) potential transient after the current step.

We further measured the impedance response in a typical SECCM setup with the droplet contacting a substrate electrode to evaluate the contribution of stray capacitance in our measurement. The equivalent circuit of the model circuit and SECCM experiment Figure S13a, and the impedance response is shown as the Nyquist plot in Figure S13b. Because the contact area of the electrode-electrolyte interface is between 0.2 and 0.5 um^2 (depending on the variations in pipette diameter, which ranges from 500 to 800 nm), the expected double-layer capacitance is between 0.04 and 0.1 pF based on a specific capacitance of 20 μF cm^{-2}. Our measured capacitance of 7 pF is much larger than this value, suggesting the stray capacitance dominates the overall capacitance, although the absolute value of 7 pF is relatively small.

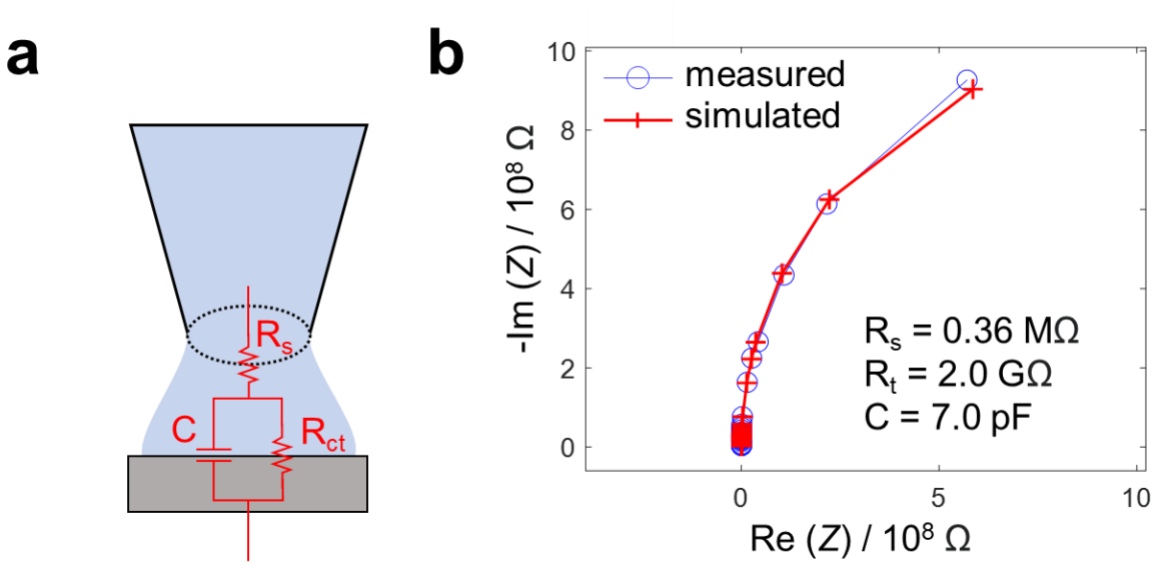

Figure S13. (a) Equivalent circuit of the Ag dissolution under SECCM. C_d is the overall capacitance, R_s is the solution resistance, and R_{ct} is the charge transfer resistance. (b) Nyquist plot during Ag dissolution at 10 pA constant current with 5 pA rms peak amplitude.

11. Monte Carlo dissolution model

This section describes the Monte Carlo (MC) simulation based on the kink site dissolution model, as mentioned in the main text. We first consider the kinetics and rate of dissolution by considering the microscopic rate at each type of site within the surface crystal lattice. We then use the geometry of the Ag lattice to describe the number of atoms in each monolayer as dissolution initiates from a perfect (100) plane.

a. Kinetic model

For simplicity, the crystal lattice is reduced to one dimension as the insights obtained are generalizable. Consider a 1-D chain of atoms. All atoms except those at the left and right extreme initially have two neighbors. These atoms with two neighbors in the 1-D model are also known as the edge atoms. The atoms at the extreme of the chain, which have only one neighbor, are known as kink sites. The rate of dissolution per atom, k_{d}, generally depends on the binding energy E_a between two neighboring atoms, and the number of neighbors, N, according to the equation:

$$k_d = \nu e^{-\left(\frac{NE_a}{k_B T}\right)} \qquad \text{S-6}$$

where $k_B$is the Boltzmann constant, T the temperature, and ν is a pre-exponential factor. The rate of dissolution for kink sites is $e^{\left(-\frac{E_a}{k_B T}\right)}$ times larger than the vs edge sites because kink sites have one less neighboring atom compared to the edge (e.g., 3.7 times larger when taking E_{a} as 1.52×10^{-20} J).[2] The rate of dissolution at a particular site *j* is the product of the number of atoms that correspond to site j, $n_{\mathrm{site\,j}}$, and the intrinsic rate of dissolution rate of each atom at site j $k_{\mathrm{site\,j}}$. The probability of dissolution at a particular site $P_{\mathrm{site\,j}}$ is the ratio of the total dissolution rate at the site j over the sum of the dissolution rates at all sites, which can be expressed as:

$$P_{\mathrm{site\,j}} = \frac{n_{\mathrm{site\,j}} k_{\mathrm{site\,j}}}{\sum_{i=1} n_{\mathrm{site\,i}} k_{\mathrm{site\,i}}} \qquad \text{S-7}$$

To track the dynamics of each site during the dissolution, an MC simulation was performed, which resulted in the fraction of different sites as a function of the degree of dissolution (i.e., fraction of atoms dissolved on one layer). The site-specific probabilities

of dissolution are considered in the MC simulation. The results are parametrized by a power function in the following form:

$$\frac{n_k}{n_{T,0}} = \alpha \left(\frac{n_T}{n_{T,0}}\right)^{\beta} \left(1 - \frac{n_T}{n_{T,0}}\right)^{\gamma} \quad \text{S-8}$$

where α, β, and γ are parametrized empirical constants (shown in red in **Figure S14**) obtained from the least square fitting of the MK simulation. n_T, represents the total number of atoms within a finite layer of silver atoms at the surface, while $n_{T,0}$, denotes the initial number of atoms within that layer. Note that this equation is also applicable to the three-dimensional case, as kink site dissolution occurs unidirectionally along edge positions, and the difference in the number of neighboring sites is the same between edges and kink sites, one. This result, that is the number of kink sites with respect to the total number of active sites during the dissolution of a finite lattice, $n_k(n_T)$, is then used to simulate the galvanostatic dissolution.

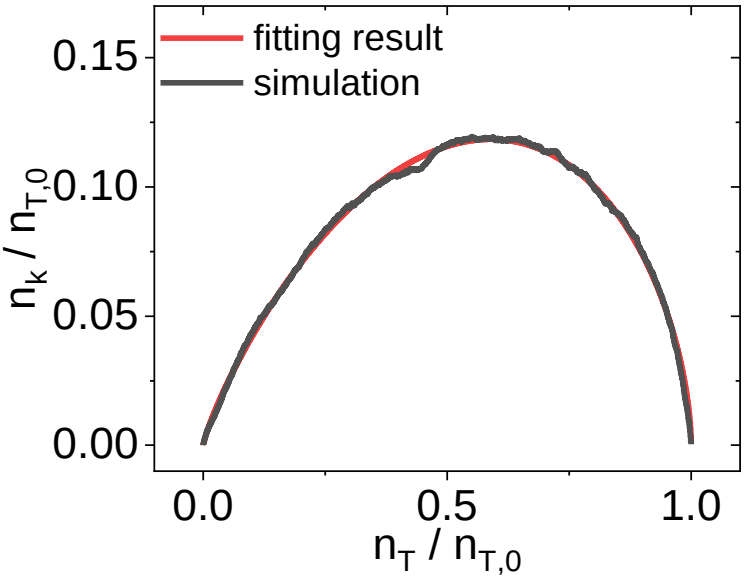

Figure S14.Monte-Carlo dissolution simulation for the kink site probability during a single layer Ag dissolution. The fitting is done with eq S-8.

b. Galvanostatic dissolution

During galvanostatic dissolution, the applied current is composed of faradic current (i_f) and non-faradaic charging current (i_c):

$$i = i_c + i_f \quad \text{S-9}$$

The faradaic current i_f is the sum of all faradaic processes at different sites. By considering a site-specific atomic exchange current, $i_{0,s}$, and multiply by the number of site-specific atoms, n_s, a Buttler-Volmer formalism can be used to relate the site-specific current and overpotential, η.

$$i_f^{\text{site j}} = n_s i_{0,s}[\exp(\alpha f\eta) - \exp(-(1-\alpha)f\eta)] \quad \text{S-10}$$

Here, overpotential η is defined as the difference between the applied potential E and equilibrium potential of the charge transfer, α is the charge transfer coefficient and f= *F/RT* is the reduced Faraday's constant. By combining equations S-8 and S-10, the kink site dissolution current, $i_{f,kink}$, is obtained, taking into account n_{kink} as defined in equation S-11:

$$i_f^{\text{kink}} = n_0^T \alpha \left(\frac{n^T}{n_0^T}\right)^{\beta} \left(1 - \frac{n^T}{n_0^T}\right)^{\gamma} i_0^{\text{kink}}[\exp(\alpha f\eta) - \exp(-(1-\alpha)f\eta)] \quad \text{S-11}$$

Where n_0^{kink} is defined as the number of atoms during the dissolution when the number of kink atoms is depleted compared to edge atoms, n_T is the number of total remaining atoms considering n_0^T as the initial number of total atoms and i_0^{kink} is the kink-site exchange current.

For edge sites the faradaic current, $i_{f,e}$ is similarly defined as:

$$i_f^{\text{edge}} = n^{\text{edge}} i_0^{\text{edge}}[\exp(\alpha f\eta) - \exp(-(1-\alpha)f\eta)] \quad \text{S-12}$$

where n_e is the number of edge atoms defined as the difference between the total number of atoms, n^T, and kink atoms (), of reacting edge atoms, andi_0^{edge} is the edge site atomic exchange current. To establish a site-specific i_0^{n} ,k_d^{n} from equation S-6 is multiplied by the elemental charge, e.

$$i_0^{\text{site j}} = ek_d^{\text{site j}} \quad \text{S-13}$$

The capacitive current, i_c, depends on the double-layer capacitance C_d and the rate of change of overpotential with respect to time $d\eta/dt$:

$$i_c = C_d \frac{d\eta}{dt} \quad \text{S-14}$$

Note that we assume the double-layer capacitance is constant vs potential. The capacitance was measured experimentally by EIS in section S10.

The initial number of total atoms in a surface layer of silver ($n_{T,0}$)is defined as N_n, from section S6, and is updated when the dissolution of the nth layer ends. Combining all the current equations yields the expression of total current:

$$i = C_d \frac{d\eta}{dt} + n_{T,0}\alpha \left(\frac{n_T}{n_{T,0}}\right)^{\beta} \left(1 - \frac{n_T}{n_{T,0}}\right)^{\gamma} i_{0,k}[\exp(\alpha f\eta) - \exp(-(1-\alpha)f\eta)] + n_e i_{0,e}[\exp(\alpha f\eta) - \exp(-(1-\alpha)f\eta)] \quad \text{S-15}$$

Rearrangement yields the expression of $\frac{d(\eta)}{dt}$:

$$\frac{d(\eta)}{dt} = \frac{i - n_{T,0}\alpha\left(\frac{n_T}{n_{T,0}}\right)^{\beta}\left(1-\frac{n_T}{n_{T,0}}\right)^{\gamma} i_{0,k}[\exp(\alpha f\eta) - \exp(-(1-\alpha)f\eta)] - n_e i_{0,e}[\exp(\alpha f\eta) - \exp(-(1-\alpha)f\eta)]}{C_d} \quad \text{S-16}$$

This equation is solved numerically to obtain a simulated *η-t* curve. The result at different applied current is shown in Figure 5e in the main text.

12. Variations of peak shape of potential transients.

In some experiments, particularly at low applied currents, the potential transients exhibit slow potential rises followed by faster decay. To further investigate this mechanism, we conducted a simulation using differential equation S-16 with one modification: after the dissolution of a single atomic layer, we introduced an induction time before the subsequent dissolution began. This effectively set the dissolution current to zero, turning the equation into:

$$\frac{d(\eta)}{dt} = \frac{i}{C_d} \qquad \text{S-17}$$

During the induction time, only capacitive current flows, causing the potential to increase linearly. Although the differential capacitance may be potential-dependent in reality, for simplicity, we assume in the model that capacitance is independent of potential. As time progresses, the potential rises due to the capacitive current until the induction period ends, at this point, dissolution resumes, sharply lowering the potential until the layer is fully dissolved. This is followed by the next induction period. Figure S15 shows how the simulated transient evolves as longer induction times are applied.

From a thermodynamic perspective, the induction time is associated with activation barriers. This means that when such transients are observed, it becomes more evident how the lack of reactive sites on the surface hinders continuous dissolution until the binding energy of the less reactive surface sites is overcome.

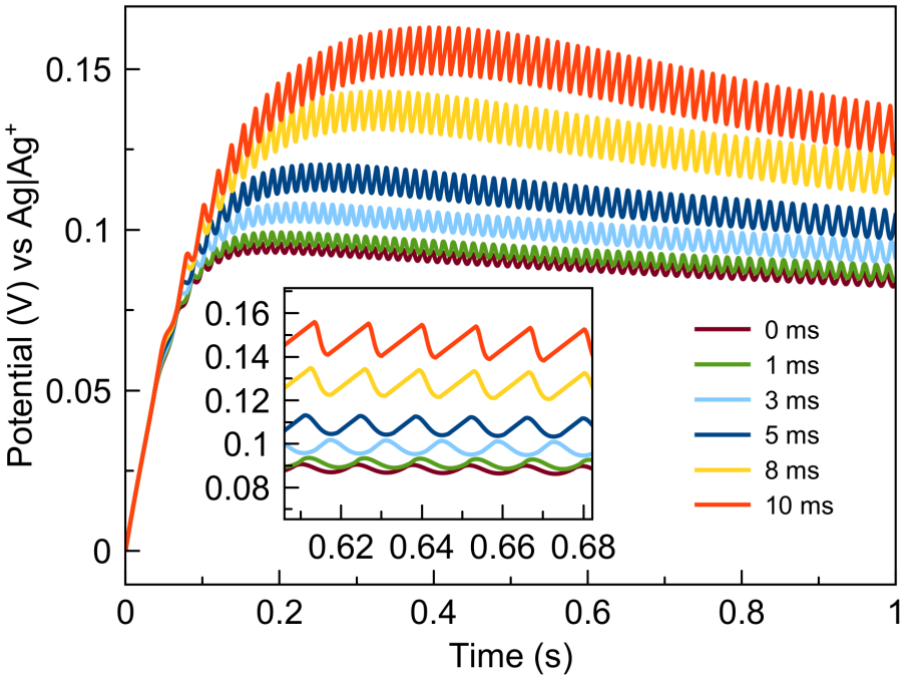

Figure S15. Galvanostatic dissolution simulation at 10 pA of applied currents with different induction times in between layer dissolution.

13. References

(1) Page, A.; Perry, D.; Unwin, P. R. *Proceedings of the Royal Society A: Mathematical, Physical and Engineering Sciences* **2017**, *473* (2200), 20160889.
(2) Chernov, A. A. *Annual Review of Materials Research* **1973**, *3* (3), 397-454.